Nanoscale

Self-Recovery in Li-Metal Hybrid Lithium-Ion Battery via WO3 Reduction

Journal:	*Nanoscale*
Manuscript ID	NR-COM-02-2018-001507.R2
Article Type:	Communication
Date Submitted by the Author:	16-Jul-2018

Complete List of Authors:	pathak, rajesh; South Dakota State University, Electrical Engineering and Computer Science Gurung, Ashim; South Dakota State University, Electrical Engineering and Computer Science Elbohy, Hytham; South Dakota State University, Center for Advanced Photovoltaics Chen, Ke; South Dakota State University Reza, Khan; SDSU, Electrical Engineering Bahrami, Behzad; South Dakota State University, mabrouk, sally; South Dakota State University, EE and CS Ghimire, Raju; South dakota state university, Electrical Engineering and Computer Science Hummel, Matthew; SDSU Gu, Zhengrong; South Dakota State University, Agricultural and Biosystems Engineering Wang, Xiaomin; Taiyuan University of Technology, College of Materials Science and Engineering Wu, Yucheng; Taiyuan University of Technology Zhou, Yue; South dakota state university, Electrical Enigneering Qiao, Qiquan; South Dakota State University, Center for Advanced Photovoltaics

Self-Recovery in Li-Metal Hybrid Lithium-Ion Battery via WO_3 Reduction

Rajesh Pathak[1], Ashim Gurung[1], Hytham Elbohy[1], Ke Chen[1], Khan Mamun Reza[1], Behzad Bahrami[1], Sally Mabrouk[1], Raju Ghimire[1], Matthew Hummel[3], Zhengrong Gu[3], Xiaoming Wang[2]*, Yucheng Wu[2]*, Yue Zhou[1]*, Qiquan Qiao[1]*

[1]Center for Advanced Photovoltaics, Department of Electrical Engineering and Computer Science, South Dakota State University, Brookings, SD 57007, USA
Tel: 1-605-688-6965; Fax: 1-605-688-4401;
yue.zhou@sdstate.edu, qiquan.qiao@sdstate.edu

[2]School of Materials Science and Engineering, Taiyuan University of Technology, Taiyuan, China
wangxiaomin@tyut.edu.cn , wyc@tyut.edu.cn

[3]Agricultural and Biosystems Engineering Department, South Dakota State University, Brookings, SD 57007, USA

Abstract

It has been a challenge to use transitional metal oxides as anode materials in Li-ion batteries due to their low electronic conductivity, poor rate capability and large volume change during charge/discharge processes. Here, we present the first demonstration of a unique self-recovery of capacity in transition metal oxide anode. This was achieved by reducing tungsten trioxide (WO_3) via the incorporation of urea, followed by annealing under nitrogen environment. The reduced WO_3 successfully self-retained the Li-ion cell capacity after undergoing a sharp decrease upon cycling. Significantly, the reduced WO_3 also exhibited excellent rate capability. While the reduced WO_3 exhibited an interesting cycling phenomenon where the capacity was significantly self-recovered after an initial sharp decrease. The quick self-recovery of 193.21%, 179.19% and 166.38% for the reduced WO_3 were observed at the 15^{th} (521.59/457.41 mAh/g), 36^{th} (538.49/536.61 mAh/g) and 45^{th} (555.39/555.39 mAh/g) cycles respectively compared to their respective preceding discharge capacity. This unique self-recovery phenomenon can be attributed to the lithium plating and conversion reaction which might be due to the activation of oxygen vacancies that act as defects which make the WO_3 electrode more electrochemically reactive with cycling. The reduced WO_3 exhibited superior electrochemical performance with

959.1/638.9 mAh/g (1st cycle) and 558.68/550.23 mAh/g (100th cycle) vs pristine WO_3 with 670.16/403.79 mAh/g (1st cycle) and 236.53/234.39 mAh/g (100th cycle) at a current density of 100 mA/g.

Keywords: Lithium ion battery, tungsten trioxide, urea, lithium plating, self-recovery.

1. Introduction

Rechargeable lithium-ion batteries (LIBs) have been monumental in applications such as portable electronics, electric vehicles and stationary grid storage [1-4]. However, the current demand of large scale energy applications of LIBs is hindered due to their low capacities and short cycling lifetime [5, 6]. To improve their capacities, electrode materials should be able to reversibly store a large amount of Li ions and exhibit fast ionic/electronic transfer performance within the cell. There are mainly three mechanisms of storing lithium ions including intercalation (e.g., graphite or lithium titanate), alloying (e.g., tin or silicon) and conversion (e.g., transitional metal oxides). Although graphite has been employed commercially as anode material for LIBs thanks to low cost and good cycling stability, the theoretical specific capacity is as low as 372 mAh/g [7]. Silicon and tin have been developed recently with higher theoretical specific capacities of 4200 mAh/g and 990 mAh/g respectively; however, they suffer from large volume expansion/contraction which is detrimental for cycling stability [8, 9].

A number of transitional metal oxides such as SnO_2 [10], Fe_3O_4 [11], MnO_2 [12], Mn_3O_4 [13], MoO_3 [14], NiO [15], and Co_3O_4 [16] have been widely investigated as LIB anodes. However, it should be noted that these materials have a poor cyclability mainly due to the electrode disintegration resulting from volume change during lithiation/de-lithiation processes[17]. Other issues in these materials include low electronic conductivity, unstable solid electrolyte interface layer and high irreversible capacity due to the formation of Li_2O [10, 13, 18, 19].

To address the issue of poor cyclability, WO_3 have attracted many interests as a potential anode for LIBs. WO_3 is a wide band gap n-type semiconductor and one of the most attractive transition metal oxides as anode materials thanks to high theoretical capacity (693 $mAhg^{-1}$), low cost and natural abundance. It also provides a higher safety for LIBs due to its intrinsic high melting temperature and strong mechanical stability [20-24]. Among anode materials of nanostructured WO_3 thin films[18], SnO_2/WO_3 core-shell[25], both Chrysanthemum-like and cookie like $WO_3 \cdot 0.33H_2O$[19, 26], WO_3 flowers comprising porous single crystalline nanoplates[27, 28], WO_3 microflowers and nanowires [28], hexagonal ultrathin WO_3 nano-ribbons[29] and WO_3 nanoparticles[30] , showed at least one of the shortcomings either the lower initial discharge or unstable capacity, lower coulombic efficiency or lower capacity retention and fast capacity fading.

Use of carbon matrix to form composite with potential anode materials has been the conventional approach to augment their electrochemical performance. Lie et al. reported a composite of WO_{3-x}/graphene synthesized in H_2/Ar atmosphere to facilitate fast Li diffusion and enhancement in electrode conductivity at high current densities[17]. Use of urea and/or N_2 doping is another approach that has been used while synthesizing anode and cathode materials in LIBs[31-37]. Previous works showed that the urea and/or N_2 doping has been used as the source of carbon to increase the catalytic activity of materials which can decrease particles sizes, introduce secondary particles, and increase the porosity in the materials, which can enhance LIB capacity and cycling performance. WO_3 making composite with carbon can lead to higher capacity due to the contribution of the capacity from carbon [17, 38]. However, in our study, no additional carbon was used to form composite with WO_3. Better catalytic performance was observed by using ammonia gas rather than using H_2 or N_2 individually[39]. However, the urea incorporation under

nitrogen annealing has not been utilized to treat WO_3 where the synergic effect of urea and N_2 doping is to create more oxygen vacancies to increase the catalytic activity and defects that reactivates within the material after number of cycling for self-recovery of capacity in LIBs.

Here, we demonstrate a unique capacity self-recovery in LIBs at constant current density using the WO_3 electrode that was reduced by incorporating urea, followed by annealing in the N_2 environment. To the best of our knowledge, this is the first discovery and demonstration of the unique capacity self-recovery in LIBs. The result suggested that urea treatment of anode materials in nitrogen atmosphere can become a promising technique, for example in silicon and other transitional metal oxides like MoO_3, to develop self-recovering high performance LIBs.

2. **Experimental Details**

2.1 Materials and Preparations

1g tungsten(VI) trioxide WO_3 (typically 99.9% pure), 1ml alpha-terpinol (Sigma-Aldrich) and 0.1g Urea 99% (Acros Organics) were mixed together to make a slurry using a mortar and pestle. The slurry of urea treated WO_3 was kept inside a tube-furnace under nitrogen flow. The temperature was maintained at 500°C for 2 h to synthesize the reduced WO_3 (R-WO_3). Pristine WO_3 is designated as P-WO_3.

Urea decomposes to ammonia at temperature ~ 180 °C and then the ammonia decomposes further at higher temperatures (> 400 °C) into N_2 gas and reactive H_2 that can reduce WO_3 and create oxygen vacancies[40-45].

$$H_2N–CO–NH_2 \longleftrightarrow NH_3 + HNCO$$

$$2NH_3 \longleftrightarrow N_2 + 3H_2$$

$$WO_3 + xH_2 \longrightarrow xH_2O + WO_{3-x}$$

2.2 Electrode fabrication

P-WO_3 and R-WO_3 powders were separately mixed with super-P carbon black and polyvinylidine fluoride (PVDF) at a weight ratio of 80:10:10 respectively in the N-Methyl-2-pyrrolidone (NMP) solvent to form slurries using the mortar and pestle. The slurry was coated on a copper foil current collector by doctor blading and then dried overnight in a vacuum oven at 100°C. The dried samples were cut into circular disks with a diameter of 12.7 mm and used as the working electrode. The total areal mass loading was typically ~2.5 mg/cm^{-2} and the areal mass loading of active material WO_3 was ~2.0 mg/cm^{-2} for both P- WO_3 and R- WO_3 electrodes.

2.3 Electrochemical characterization

CR-2032 Li-ion coin cell was assembled using lithium metal as the counter and reference electrode inside an argon-filled glove box. Celgard was used as separator and liquid electrolyte consisted of 1M $LiPF_6$ dissolved in a solvent mixture of ethylene carbonate, dimethyl carbonate and diethyl carbonate in the volume ratio of 4:2:4.

X-ray diffractogram (XRD) and crystallite size measurements of the samples were conducted on a Rigaku SmartLab diffractometer with Cu-Kα radiation (λ=1.54178 Angstrom). Topography of thin films were measured using Agilent SPM 5500 atomic force microscope (AFM) equipped with MAC III controller using a tip with resonance frequency of 75 kHz. Scanning electron microscopy (SEM) and energy dispersive X-ray spectroscopy (EDS) characterization were carried out using a Hitachi S-4300 N SEM. Isotherm adsorption analysis with N_2 were carried out using an ASAP 2020 Micropore Analyzer at 77 K (liquid nitrogen bath). Brunauer-Emmett-Teller (BET) equation was used to calculate the specific surface areas. The absorption characterization was performed using Agilent 8453 UV-vis spectrophotometer. For this, 0.1g of each P-WO_3 and R-WO_3 powder was dissolved separately in aqueous solution

of nitric acid with 1:1 volume ratio. Tauc's plots were obtained using Tauc's equation $\alpha h\nu = A(h\nu - E_g)^n$, where A is constant, hν is photon energy, E_g is band gap, α is absorption coefficient and n (1/2 for WO_3) is exponent coefficient which denotes the nature of electron transition from valence to conduction band. Cyclic voltammetry (CV) was measured by an electrochemical workstation (Ametek VERSASTAT3-200 potentiostat) having a potential range of 0.01V- 3.0V at a scan rate of 0.0002V/s. The electrochemical impedance spectroscopy (EIS) was done using the same electrochemical workstation with a 10mV amplitude AC signal with the frequency ranging from100 kHz to 0.01 Hz. Galvanostatic charge-discharge measurements of the coin cells were carried out using LAND CT2001A system in a potential range of 0.01-3.0 V (vs Li^+/Li) at a current density of 100 mA/g.

3. Results and Discussions

3.1 Structural characterization

Figure 1a shows XRD patterns of the P-WO_3 and R-WO_3. The sharp peaks strongly indicate that P-WO_3 is crystalline in nature. The peaks of P-WO_3 can be indexed as monoclinic crystalline phase WO_3 (JCPDS file no. 43-1035) [46, 47]. As shown in Figure 1a, the peaks became broader for R-WO_3 suggesting a transition to amorphous nature that can be attributed to the defects created by oxygen vacancies in R-WO_3 [48, 49]. The monoclinic diffraction peaks as seen in P-WO_3 disappeared with emergence of some new peaks for R-WO_3. The peaks showing the planes (120), (112), (122), (222), (321), (004), (240), (340), (414) and (422) at 2θ of ~ 26°, 28°, 36°, 41.8°, 44°, 46°, 63°, 71° and 77° respectively in the P-WO_3 disappeared in the R-WO_3. The new peaks at the 2θ of ~ 41°, ~54° and ~ 58° (indicated by #) for R-WO_3 have been indexed as the monoclinic $WO_{2.9}$ (JCPDS file no. 05-0386) and that at the 2θ of ~ 48° (indicated by *) as the monoclinic $WO_{2.92}$ (JCPDS file no. 30-1387). The appearance of these new peaks, similar to

previous reports[17, 49, 50], is an indication of successful reduction of WO_3. Similarly, figure 1b shows the Raman spectra for R -WO_3 and P-WO_3. The four main peaks at ~264 cm^{-1}, ~324 cm^{-1}, ~710 cm^{-1} and ~801 cm^{-1} can be attributed to the monoclinic crystal structure of WO_3. For R-WO_3, the Raman peaks become broader indicating the formation of an amorphous phase of WO_3 that can be attributed to the oxygen vacancies[45, 49].

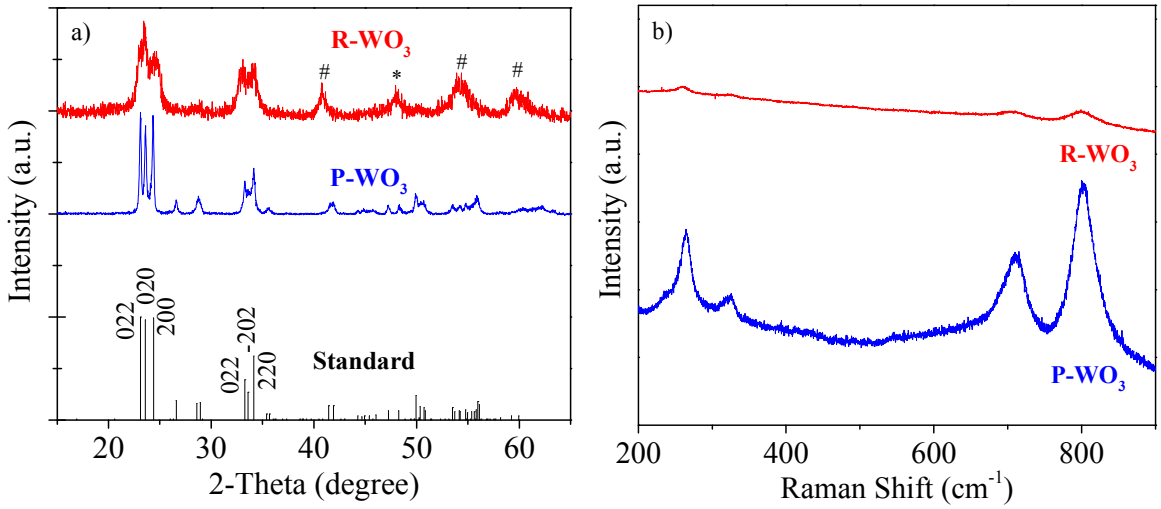

Figure 1. a) XRD patterns and **b)** Raman spectra for P -WO_3 and R-WO_3

The crystallite size (τ) of P-WO_3 and R-WO_3 was estimated using Scherrer equation: $\tau = K\lambda/\beta \cos\theta$, where θ is the usual Bragg angle, λ is the radiation wavelength, β is peak width and K is a constant at 0.9. The crystallite sizes estimated from the main peaks of the planes (020), (220) and (022) of WO_3 are summarized in Table 1 and the estimated crystallite size from each 2-theta angle is summarized in supporting information (Table S1). The crystallite size was smaller for R-WO_3 compared to P-WO_3 can be attributed to the impact of calcination in inert atmosphere[51]. This smaller crystallite size for R-WO_3 improves the kinetics of lithium ions, thereby shortening their diffusion path lengths which lead to higher coulombic efficiency and capacity in LIBs [51-54].

Table 1. Estimated crystallite size

sample	2θ (°)	crystallite size (nm)
P-WO_3	23.59	463
R-WO_3	23.45	94
P-WO_3	24.37	395
R-WO_3	24.69	62
P-WO_3	33.27	81.1
R-WO_3	33.28	45.4

Figures 2a, b show the AFM topography images of P-WO_3 and R-WO_3, respectively. It is obvious that the particles of the P-WO_3 are larger than those of R-WO_3. The time for insertion/deinsertion decreases with the square of the decrease in particle size[55]. In order to demonstrate the surface area increase, BET specific surface area measurement was carried out. The BET specific surface area (SSA) of P-WO_3 and R-WO_3 was calculated to be 4.59 m^2/g and 47.59 m^2/g respectively. The N_2 adsorption-desorption isotherms of P-WO_3 and R-WO_3 powder sample are shown in supporting information Figure S4. This decrease in the particle size increases the surface area of R-WO_3, giving rise to the enhancement of active sites of the anode [19, 56]. The rate of lithium insertion/deinsertion increases due to shoter distances for lithium-ion transport within the particles and further, high surface area allows better surface contact with the electrolyte to enhance the lithium ion flux across the interface[56]. Figures 2 e, h show the SEM images of P-WO_3 and R-WO_3 along with elemental mapping images of oxygen, O (figs. 2f, i) and tungsten, W (figs. 2g, j) respectively. The elemental mapping images show that O and W elements are homogeneously distributed across both P-WO_3 and R-WO_3. The EDS images for P-WO_3 and R-WO_3 are shown in supporting information Figures S1, S2 respectively. Table 2 represents the percentage concentrations by weight of W and O in the P-WO_3 and R-WO_3. The

percentage concentration by weight of W and O in P-WO_3 were found to be 78.26% and 21.74% respectively, while R-WO_3 showed 80.28% and 19.72% respectively. It can be seen that the oxygen concentration was reduced in R-WO_3 compared to P-WO_3. This reduction indicates the successful reduction of WO_3 to WO_{3-x}.

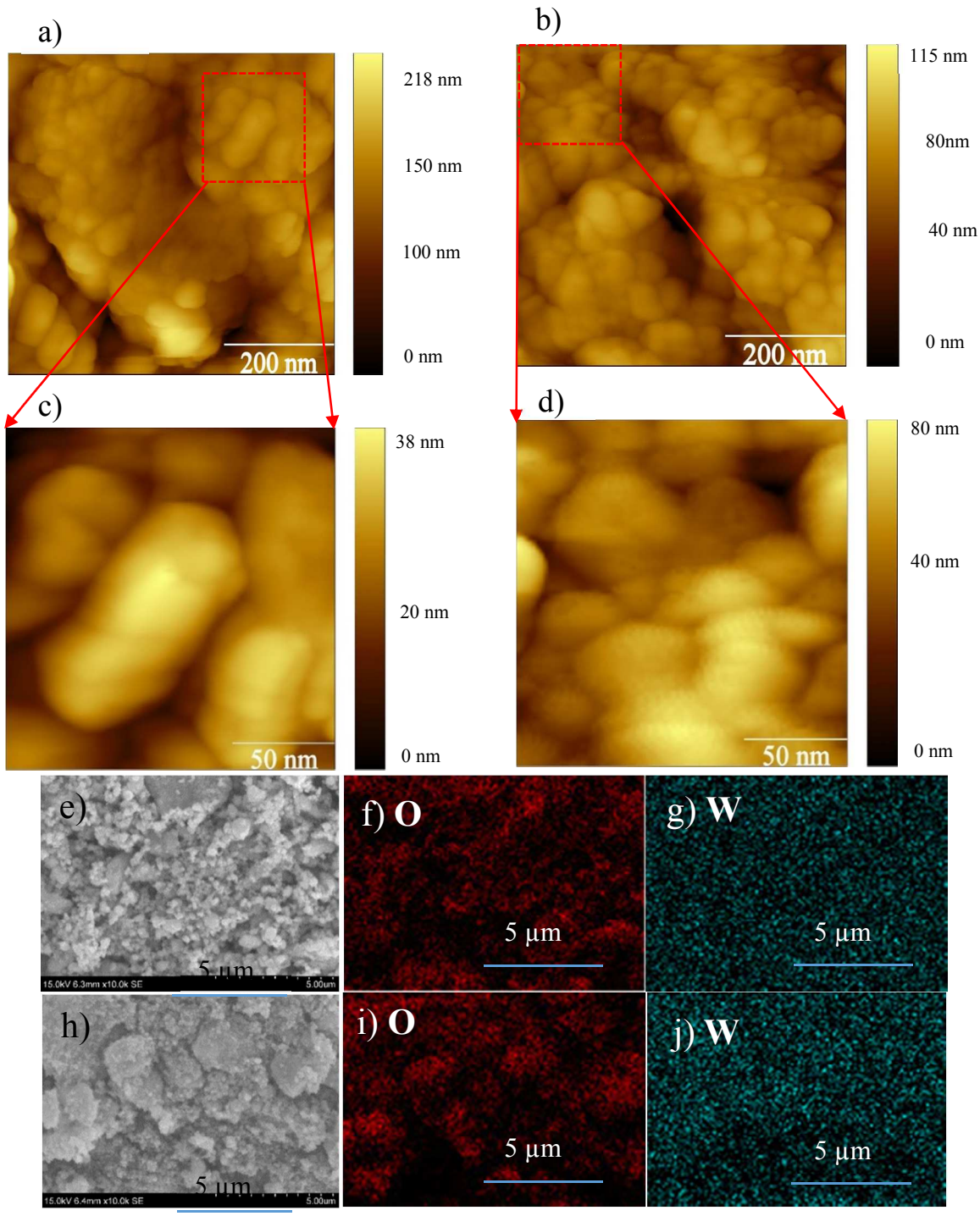

Figure 2. AFM topography images of **a)** P-WO_3 and **b)** R-WO_3, **c), d)** High magnification AFM image of P-WO_3 and R-WO_3 respectively; **e)** SEM image of P-WO_3

with EDS mapping of **f)** O and **g)** W; **h)** SEM image of R-WO_3 with EDS mapping of **i)** O and **j)** W.

Table 2. Percentage concentration by weight of W and O in P-WO_3 and R-WO_3.

WO_3	**Element**	**Line**	**Intensity(c/s)**	**Error2-sig**	**Conc.**	**Units**
Pristine	O	Kα	69.78	1.245	21.739	wt%
	W	Lα	18.91	0.648	78.261	wt%
Reduced	O	Kα	67.93	1.229	19.718	wt%
	W	Lα	21.23	0.687	80.282	wt%

Optical properties of P-WO_3 and R-WO_3 were investigated to determine the effect of oxygen deficiencies. Figure 3 shows *Tauc*'s plots for P-WO_3 and R-WO_3 to find their optical bandgap (E_g). The absorption coefficient α due to interband transition near the band gap is well described by the *Tauc's* equation in which the intercept of tangent to the curve with the x-axis determines the value of the optical band gap ***(E_g)***[57]. R-WO_3 has an E_g of ~2.32 eV, while P-WO_3 has an E_g of ~2.85 eV. This decrease in band gap might be attributed to the introduction of oxygen vacancies inside urea activated N_2 annealed R-WO_3 [58-60]. The lower bandgap suggests a higher electronic conductivity in R-WO_3, which can enhance the capacity in LIBs [61]. Inset in figure 3 shows the optical images of (A) P-WO_3 and (B) R-WO_3. The light yellowish green color of P-WO_3 turned into dark blue after the reduction of WO_3 by urea activation under the N_2 annealing at 500°C which supports the band gap reduction.

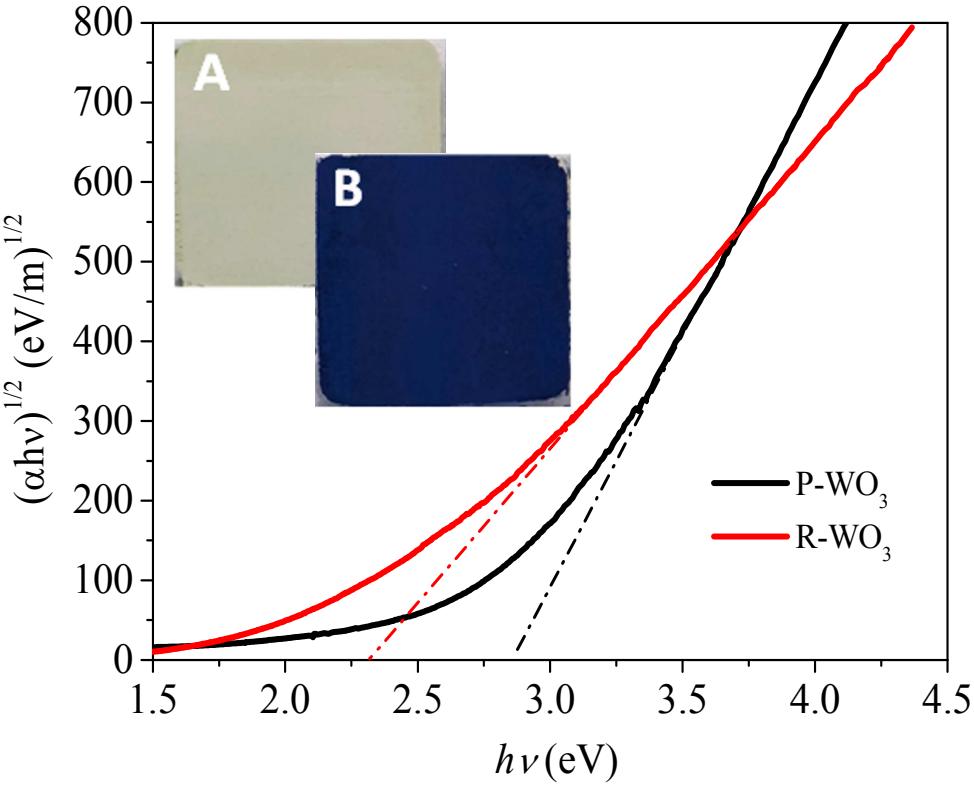

Figure 3. Tauc plot for P-WO_3 and R-WO_3. Inset: optical images of **(A)** P-WO_3 and **(B)** R-WO_3

3.2 Electrochemical Performance

Figures 4a and 4c show cyclic voltammograms of P-WO_3 and R-WO_3 electrodes respectively. In the 1st cycle, the cathodic peaks were observed at 2.3 V, 0.59 V and 0.01 V during the lithiation for both electrodes. The peak at 2.3 V is attributed to the partial lithiation of WO_3 to Li_xWO_3 while the peak at 0.59 V corresponds to the conversion reaction which converts Li_xWO_3 to W and Li_2O and the formation of SEI layer [18]. The reduction peak at 0.01 V represents the reduction of W cation to W^0 which can be expressed by the second equation given below [62, 63]. Similarly, the anodic peaks were observed at 1.2 V and 2.0 V during delithation. The peak at 1.2 V corresponds to the oxidation reaction of W to Li_xWO_3; the peak at 2.0 V corresponds to the formation of WO_3 from Li_xWO_3 [62]. It can be observed that the intensity of both reduction and oxidation peaks of R-WO_3 were higher than that of P-WO_3. In addition, the

R-WO_3 exhibited comparable intensities of reduction and oxidation peaks even for the 10th and 35th cycles whereas P-WO_3 exhibited no relevant peaks. This indicates that the urea incorporated annealing technique improved the electrochemical activity and cyclic stability of the WO_3 electrode. The charge and discharge mechanisms are illustrated below.

$$WO_3 + xLi^+ + xe^- \leftrightarrow Li_xWO_3 \ldots\ldots\ldots (1)$$

$$Li_{1.1}WO_3 + 4.9Li^+ + 4.9e^- \leftrightarrow W + 3Li_2O \ldots\ldots\ldots (2)$$

The electrochemical performance of P-WO_3 and R-WO_3 was characterized by galvanostatic charge/discharge tests at a constant current density of 100 mA/g and voltage profiles of P-WO_3 and R-WO_3 are shown in figures 4b and 4d. The Li^+ ions electrochemically react with WO_3 in multiple steps and can be observed by the appearance of the voltage plateaus at 2.3V, 0.59 V and 0.01 during lithiation and 1.2V and 2.0V during delithiation. For the 1st discharge, a small sloping voltage was observed at 2.3 V which corresponds to the lithiation of WO_3 to Li_xWO_3, followed by a plateau 0.59 V due to the conversion of Li_xWO_3. The plateau at 0.01 V corresponds to the conversion of W cation to W^0 [62, 63]. Similarly, for the charging, the sloping voltage at 1.2 V corresponds to the oxidation of W to Li_xWO_3; the peak at 2.0 V corresponds to formation of WO_3 from Li_xWO_3 [62]. For higher cycles at 100 mA/g, R-WO_3 still exhibited sloping voltage profile while the P-WO_3 showed sharp slope voltage profiles indicating surface storage as complemented by the C-V measurements for higher cycles.

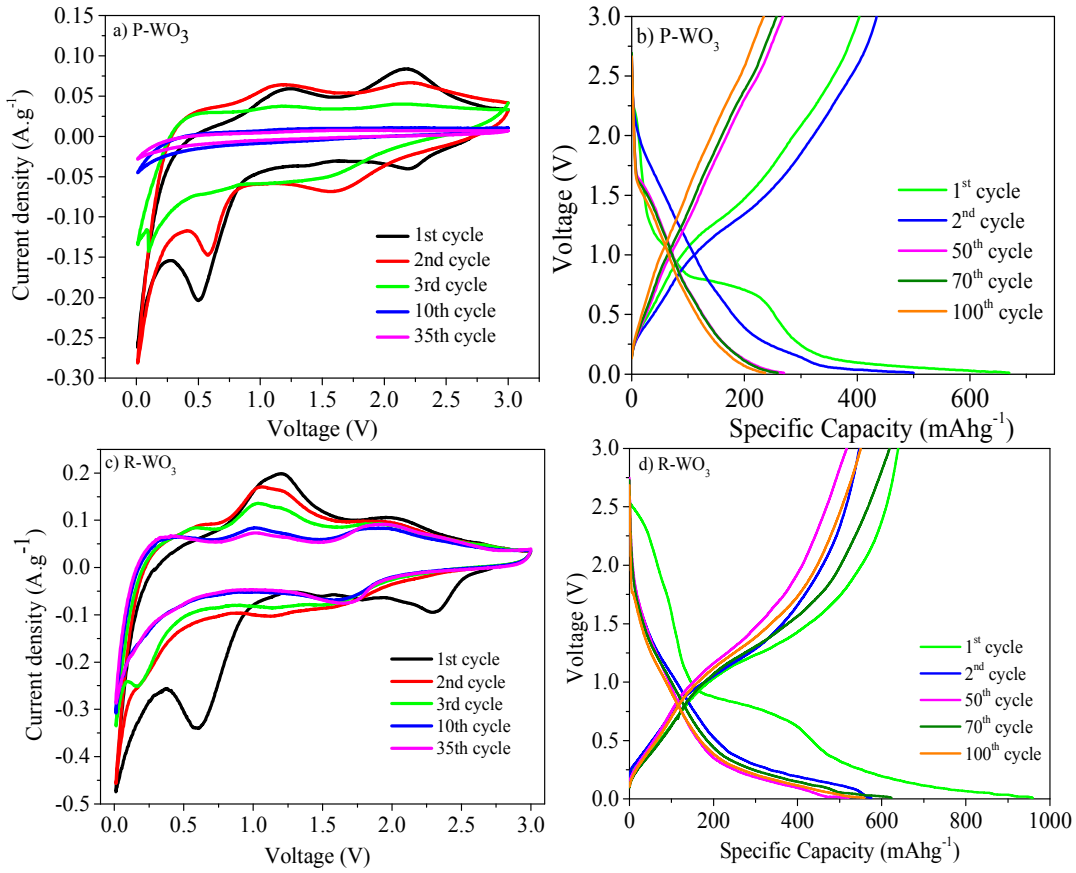

Figure 4. Cyclic voltammograms of **(a)** P-WO_3, **(c)** R-WO_3 and Galvanostatic charge/discharge voltage profiles of **(b)** P-WO_3, **(d)** R-WO_3 at 100 mA/g.

At constant current density of 100 mA/g (Figure 5 a) , P-WO_3 and R-WO_3 anodes delivered an initial discharge capacity of 670.16 mAh/g and 959.15 mAh/g exhibiting coulombic efficiency of 60.25% and 66.62% respectively. The discharge capacities for P-WO_3 and R-WO_3 were reduced to 500 mAh/g and 575.1 mAh/g in the following 2^{nd} cycle, respectively. The initial irreversible capacity loss might be attributed to decomposition of electrolyte and the formation of solid-electrolyte interface (SEI) layer on the electrode surface[64]. The P-WO_3 exhibited a sharp decrease in the capacity for the first 10 cycles and poor cycling performance with a decrease of discharge capacity from 670.16 mAh/g for the 1^{st} cycle to 236.5 mAh/g for the 100^{th} cycle. However, the R-WO_3 exhibited an interesting cycling phenomenon where the capacity was significantly recovered and self-retained after the initial sharp decrease. The self-recovery for R-

WO_3 were observed at the 15th (521.59/457.41 mAh/g), 36th (538.49/536.61 mAh/g), 45th (555.39/555.39 mAh/g) cycles with gradual increase in the capacity after the 54th cycle to as high as 623.5/618.77 mAh/g at 70th cycle and a steady 558.68/550.23 mAh/g at 100th cycle. The respective self-recovery at 15th, 36th and 45th was 193.21%, 179.19% and 166.38% compared to their respective preceding discharge capacity. However, no such self-recovery phenomenon was observed for P-WO_3. The observation of sloping discharge voltage plateau from 0.75 V to 0.002 V corresponds to the common conversion reaction of WO_3[63, 65]. The sloping plateau near 0.01 V can be attributed to the further lithiation of lithiated WO_3 which corresponds to the complete reduction of W cation to W^o [62, 63]. The flat nature of discharge plateau at ~0.01 V can be attributed to the lithium plating as confirmed by SEM images and XRD pattern provided in the supporting information (Figure S5). Figures S5a, b in the supporting information show the cycling performances up to 17th discharge that presented capacity self-recovery and corresponding voltage profile respectively. Figures S5c, d and e show the SEM images and corresponding XRD patterns of R-WO_3 electrode on copper current collector before cycling and at 17th discharge respectively. The SEM images show the presence of a dense surface and XRD confirms the surface consists of plated lithium. Similar observation of Li plating and Li ion intercalation on graphite encapsulated Li-metal hybrid anode battery was observed by Sun et al.[66]. Thus, self-recovery of capacity in R-WO_3 can be attributed to the lithium plating and conversion reaction. This self-recovery phenomenon observed in R-WO_3 can be attributed to the insufficient crystallinity and existence of further activation process caused by the impurity or surface defects of the anode electrode calcined in N_2 atmosphere at high temperature due to accelerating ion movement [37, 67, 68]. Generally, the plating of lithium on anode material that occurs during over charge/discharge, at high current rates and charging/discharging at low

temperature is considered a major safety concern. However, the R-WO_3 in this work, even after lithium plating demonstrated excellent coulombic efficiency as shown in Figure 5c. This new finding can open door to other opportunities exploring lithium plating to get higher capacities. The enhanced capacity in R-WO_3, due to O_2 vacancy, can be attributed to the lower band gap and improvement in charge transfer kinetics due to lower charge transfer resistance as observed in tauc's plot and Nyquist plot respectively. The voltage profile plots in the supporting information (Figure S3) showed that the behavior of capacity self-recovery in R-WO_3 is mainly from the lithium ions storage in R-WO_3 and lithium plating at around 0.01V.

Similarly, Figure 5b shows the rate capability performance of P-WO_3 and R-WO_3 at current densities of 35 mA/g, 70 mA/g, 140 mA/g, 280 mA/g and again at 35 mA/g for 5 cycles each and the discharge/charge capacities are summarized in Table 3. It can be noted that the R-WO_3 exhibited superior rate capability performance compared to P-WO_3 with higher discharge/charge capacities for all the different current densities. A recovery of 633.7/645.7 mAh/g specific capacity at 35 mA/g was observed for R-WO_3 which accounted for 94.22% of the 2nd specific charge capacity. In comparison, P-WO_3 retained only 354.7/371.4 mAh/g accounting for 87.96%. This capacity recovery shows that the R-WO_3 has excellent electrochemical reversibility and stability structure compared with P-WO_3. Moreover, the R-WO_3 had superior coulombic efficiencies compared to P-WO_3 mostly in the initial cycles as shown in Figures 5c,d. Figures 5e,f show the voltage profiles at different current densities for P-WO_3 and R-WO_3 respectively. At higher current densities, the R-WO_3 still exhibited sloping voltage profiles as that observed for the low current density whereas, the P-WO_3 exhibited profiles indicating only surface storage. This improvement in the capacity for R-WO_3 can be attributed to the higher electrochemical catalytic activity resulting from higher surface area and

more active sites in R-WO_3 with smaller crystallite sizes. This shortens the Li ion diffusion path length and promotes the sufficient electrode/electrolyte interface for the reaction [31, 32, 34, 54, 67, 69]. The self-recovery of the capacity can be attributed to the reactivation of active sites of reduced WO_3 due to oxygen vacancies that act as defects, making the WO_3 electrode more electrochemically reactive with cycling[32, 70].

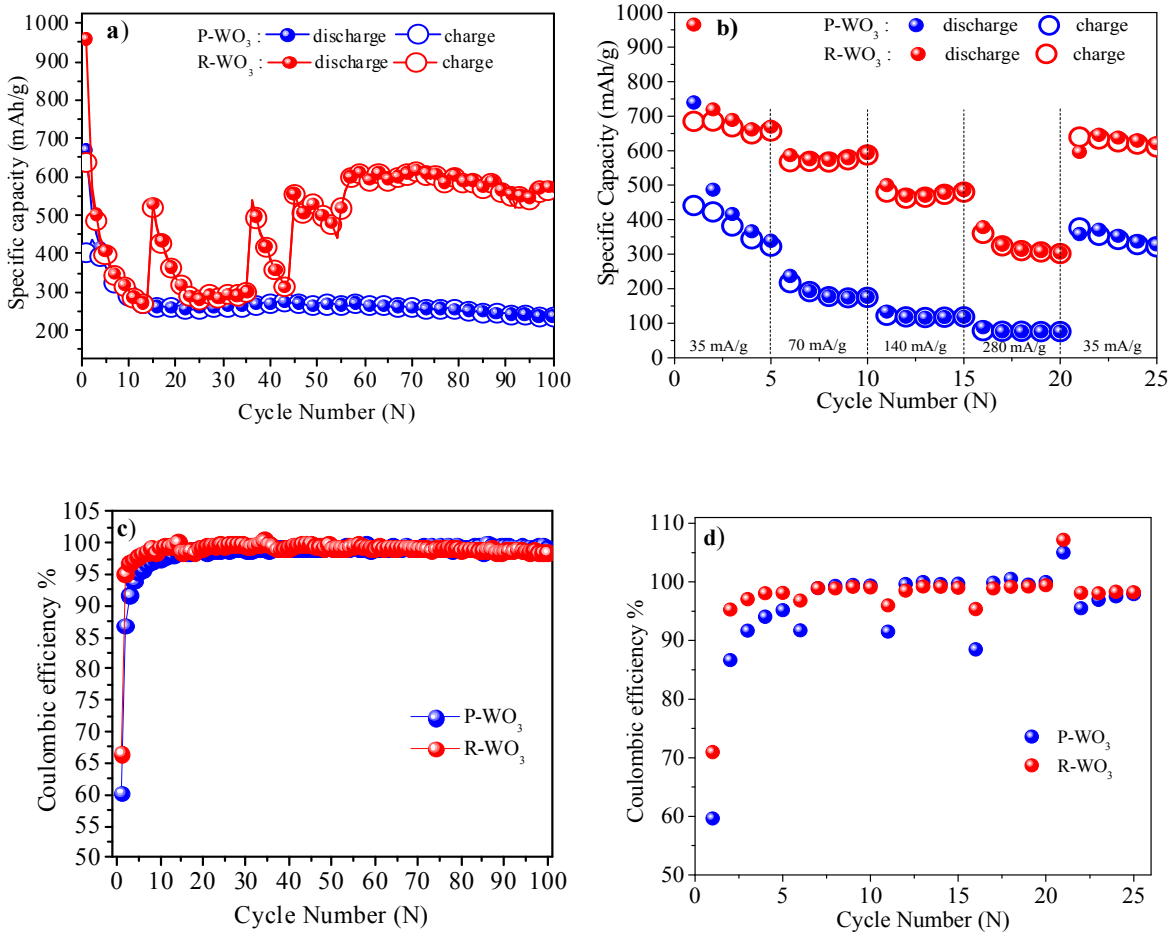

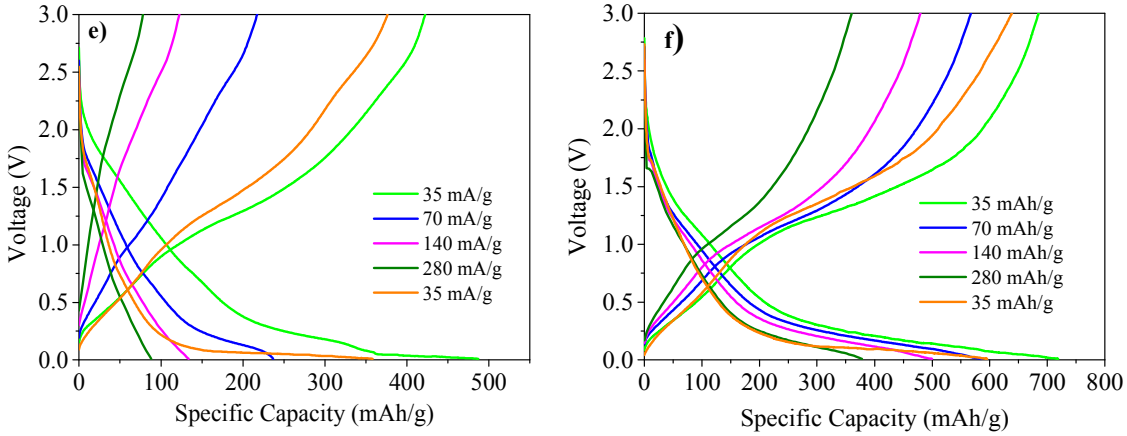

Figure 5. Cycling performance of P-WO_3 and R-WO_3 at constant current density **a)** specific capacity and **c)** coulombic efficiency; Rate capability of P-WO_3 and R-WO_3 **b)** specific capacity and **d)** coulombic efficiency; Charge-discharge voltage profiles at different current densities **e)** P-WO_3 and **f)** R-WO_3.

Table 3. Comparison of capacities of P-WO_3 and R-WO_3 at different current densities.

Cycle number	**Current density (mA/g)**	**Discharge/charge capacity (mAh/g)**	
		P-WO_3	**R-WO_3**
1st	35	739.6/441.1	964.9/684.6
2nd	35	487.2/422.2	719.2/685.3
6th	70	237.0/217.4	586.7/568.0
11st	140	133.7/122.4	500.3/480.1
16th	280	88.3/87.1	378.2/360.7
22nd	35	354.7/371.4	633.7/645.7

Electrochemical impedance spectroscopy (EIS) characterization was carried out to investigate electrical conductivity and electrochemical kinetics of P-WO_3 and R-WO_3 electrodes. Figure 6 shows the Nyquist plots of the two electrodes with a potential window of 0.01-3.0 V with frequency ranging from100 KHz to 0.01 Hz. In the Nyquist plot, the Z-real axis corresponds to the ohmic or series resistance (R_s) which is the total resistance of the electrolyte, separator, electrodes, spacer, spring and the casing. The semicircle in lower frequency range gives the charge transfer resistance (R_{ct}) at the electrode/electrolyte interface and the constant phase

element (*CPE*) represents the electric double layer capacitance of the electrode/electrolyte interface and SEI film capacitance. The inclined line in the lower frequency region corresponds to Warburg impedance (W) which represents to the lithium-ion diffusion or Warburg diffusion in the cell [71]. The equivalent circuit used for fitting of the experimental data is shown in figure 6 inset. The R_{ct} for P-WO_3 and R-WO_3 were 1195 Ω and 135.1 Ω respectively. This lower R_{ct} in R-WO_3 indicates the improvement in charge transfer kinetics of R-WO_3, which can be attributed to its smaller crystallite size and larger BET specific surface area (47.59 m^2/g for R-WO3 vs 4.59 m^2/g for P-WO_3) and allows better surface contact with the electrolyte to enhance the lithium ion flux across the interface[56, 72]. In addition, the synergic effect of H_2 and N_2 creates more oxygen vacancies and active sites in R-WO_3. This provides a shallow electron donor for R-WO_3 introducing the band gap narrowing, facilitates easy charge transportation and improves the catalytic activity[39, 45, 48, 58, 60].

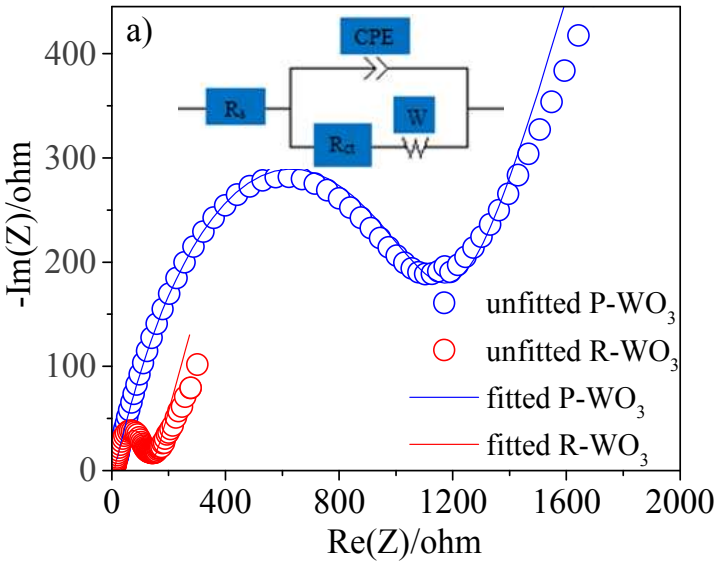

Figure 6. Nyquist plots of P-WO_3 and R-WO_3 electrodes. Inset: equivalent electrical circuit used for fitting.

4. Conclusions

In summary, in this work, we demonstrated a unique capacity self-recovery technique in a transition metal oxide anode based Li-ion battery. This was achieved using a novel technique to reduce WO_3 by incorporating urea into WO_3 under nitrogen annealing. The reduced WO_3 exhibited superior cycling capacities via self-recovery with improved rate capabilities over pristine WO_3. The self-recovery characteristics of the reduced WO_3 were attributed to lithium plating and conversion reaction due to larger surface area and the activation of oxygen vacancies that act as defects and make the WO_3 electrode more electrochemically reactive. Similar technique can be used for other high capacity battery materials to improve their electrochemical reactivity, capacity and stability.

Acknowledgement

We acknowledge the financial support from NASA EPSCoR and NSF MRI.

References

1. Gurung, A., et al., *Highly Efficient Perovskite Solar Cell Photocharging of Lithium Ion Battery Using DC–DC Booster.* Advanced Energy Materials, 2017. **7**(11): p. 1602105-n/a.
2. Zhou, Z., et al., *Binder Free Hierarchical Mesoporous Carbon Foam for High Performance Lithium Ion Battery.* Scientific Reports, 2017. **7**(1): p. 1440.
3. McGraw, M., et al., *One-step solid-state in-situ thermal polymerization of silicon-PEDOT nanocomposites for the application in lithium-ion battery anodes.* Polymer, 2016. **99**: p. 488-495.
4. Gurung, A. and Q. Qiao, *Solar Charging Batteries: Advances, Challenges, and Opportunities.* Joule, 2018.
5. Lin, D., Y. Liu, and Y. Cui, *Reviving the lithium metal anode for high-energy batteries.* Nature nanotechnology, 2017. **12**(3): p. 194.
6. Naderi, R., et al., *Activation of Passive Nanofillers in Composite Polymer Electrolyte for Higher Performance Lithium-Ion Batteries.* Advanced Sustainable Systems, 2017. **1**(8).
7. Wu, Y.-P., et al., *Anode materials for lithium ion batteries by oxidative treatment of common natural graphite.* Solid State Ionics, 2003. **156**(3): p. 283-290.
8. Chan, C.K., et al., *High-performance lithium battery anodes using silicon nanowires.* Nature nanotechnology, 2008. **3**(1): p. 31-35.

9. Gurung, A., et al., *Tin selenide–multi-walled carbon nanotubes hybrid anodes for high performance lithium-ion batteries.* Electrochimica Acta, 2016. **211**: p. 720-725.
10. Park, M.S., et al., *Preparation and Electrochemical Properties of SnO2 Nanowires for Application in Lithium-Ion Batteries.* Angewandte Chemie, 2007. **119**(5): p. 764-767.
11. Taberna, P.-L., et al., *High rate capabilities Fe3O4-based Cu nano-architectured electrodes for lithium-ion battery applications.* Nature materials, 2006. **5**(7): p. 567-573.
12. Reddy, A.L.M., et al., *Coaxial MnO2/carbon nanotube array electrodes for high-performance lithium batteries.* Nano letters, 2009. **9**(3): p. 1002-1006.
13. Varapragasam, S.J., et al., *Kirkendall Growth of Hollow Mn3O4 Nanoparticles upon Galvanic Reaction of MnO with Cu2+ and Evaluation as Anode for Lithium-Ion Batteries.* The Journal of Physical Chemistry C, 2017. **121**(21): p. 11089-11099.
14. Hassan, M.F., et al., *Carbon-coated MoO_3 nanobelts as anode materials for lithium-ion batteries.* Journal of Power Sources, 2010. **195**(8): p. 2372-2376.
15. Varghese, B., et al., *Fabrication of NiO nanowall electrodes for high performance lithium ion battery.* Chemistry of Materials, 2008. **20**(10): p. 3360-3367.
16. Wang, G., et al., *Cobalt oxide–graphene nanocomposite as anode materials for lithium-ion batteries.* Journal of Solid State Electrochemistry, 2011. **15**(11-12): p. 2587-2592.
17. Liu, F., et al., *A mesoporous WO3− X/graphene composite as a high-performance Li-ion battery anode.* Applied Surface Science, 2014. **316**: p. 604-609.
18. Li, W.-J. and Z.-W. Fu, *Nanostructured WO 3 thin film as a new anode material for lithium-ion batteries.* Applied Surface Science, 2010. **256**(8): p. 2447-2452.
19. Poizot, P., et al., *Nano-sized transition-metal oxides as negative-electrode materials for lithium-ion batteries.* Nature, 2000. **407**(6803): p. 496-499.
20. Kim, D.-M., et al., *Two-dimensional nanocomposites based on tungsten oxide nanoplates and graphene nanosheets for high-performance lithium ion batteries.* Electrochimica Acta, 2015. **163**: p. 132-139.
21. Pervez, S.A., et al., *Anodic WO3 mesosponge@ carbon: A novel binder-less electrode for advanced energy storage devices.* ACS applied materials & interfaces, 2015. **7**(14): p. 7635-7643.
22. Sasidharan, M., et al., *WO 3 hollow nanospheres for high-lithium storage capacity and good cyclability.* Nano Energy, 2012. **1**(3): p. 503-508.
23. Sim, C.M., Y.J. Hong, and Y.C. Kang, *Electrochemical Properties of Yolk-Shell, Hollow, and Dense WO3 Particles Prepared by using Spray Pyrolysis.* ChemSusChem, 2013. **6**(8): p. 1320-1325.
24. Huang, K. and Q. Zhang, *Rechargeable lithium battery based on a single hexagonal tungsten trioxide nanowire.* Nano Energy, 2012. **1**(1): p. 172-175.
25. Xue, X.-Y., et al., *SnO2/WO3 core–shell nanorods and their high reversible capacity as lithium-ion battery anodes.* Nanotechnology, 2011. **22**(39): p. 395702.
26. Yang, J., et al., *Facile preparation and electrochemical properties of hierarchical chrysanthemum-like WO 3· 0.33 H 2 O.* Journal of Materials Chemistry, 2012. **22**(9): p. 3699-3701.
27. Qiu, Y., et al., *Hierarchical WO 3 flowers comprising porous single-crystalline nanoplates show enhanced lithium storage and photocatalysis.* Nano research, 2012. **5**(11): p. 826-832.

28. Liu, Y., et al., *Rational design of WO3 nanostructures as the anode materials for lithium-Ion batteries with enhanced electrochemical performance.* Nano-Micro Letters, 2015. **7**(1): p. 12-16.
29. Lian, C., et al., *Preparation of hexagonal ultrathin WO3 nano-ribbons and their electrochemical performance as an anode material in lithium ion batteries.* Nano Research, 2016. **9**(2): p. 435-441.
30. Santhosha, A., S.K. Das, and A.J. Bhattacharyya, *Tungsten Trioxide (WO3) Nanoparticles as a New Anode Material for Sodium-Ion Batteries.* Journal of Nanoscience and Nanotechnology, 2016. **16**(4): p. 4131-4135.
31. Zhao, C., et al., *Urea-assisted combustion synthesis of porous Li1. 2Ni0. 13Co0. 13Mn0. 54O2 microspheres as high-performance lithium-ion battery cathodes.* Micro & Nano Letters, 2015. **10**(11): p. 662-665.
32. Qie, L., et al., *Nitrogen-doped porous carbon nanofiber webs as anodes for lithium ion batteries with a superhigh capacity and rate capability.* Advanced materials, 2012. **24**(15): p. 2047-2050.
33. Kim, K.-Y., Y. Jung, and S. Kim, *Study on urea precursor effect on the electroactivities of nitrogen-doped graphene nanosheets electrodes for lithium cells.* CARBON LETTERS, 2016. **19**(1): p. 40-46.
34. Sharma, Y., et al., *Li-storage and cyclability of urea combustion derived ZnFe 2 O 4 as anode for Li-ion batteries.* Electrochimica Acta, 2008. **53**(5): p. 2380-2385.
35. Mohan, E.H., et al., *Urea and sucrose assisted combustion synthesis of LiFePO4/C nano-powder for lithium-ion battery cathode application.* AIMS Materials Science, 2014. **1**(4): p. 191-201.
36. Zhou, G., et al., *Long-life Li/polysulphide batteries with high sulphur loading enabled by lightweight three-dimensional nitrogen/sulphur-codoped graphene sponge.* Nature communications, 2015. **6**.
37. Yang, K., et al., *Urea combustion synthesis of LiNi 0.5 Mn 1.5 O 4 as a cathode material for lithium ion batteries.* Particuology, 2012. **10**(6): p. 765-770.
38. Gao, H., et al., *Synthesis and Electrochemical Properties of Nano WO3/C Composite for Lithium-Ion Batteries.* ECS Transactions, 2014. **62**(1): p. 9-18.
39. Song, D., et al., *NH 3-treated WO 3 as low-cost and efficient counter electrode for dye-sensitized solar cells.* Nanoscale research letters, 2015. **10**(1): p. 16.
40. Lendzion-Bielun, Z., U. Narkiewicz, and W. Arabczyk, *Cobalt-based catalysts for ammonia decomposition.* Materials, 2013. **6**(6): p. 2400-2409.
41. Bell, T. and L. Torrente-Murciano, *H2 production via ammonia decomposition using non-noble metal catalysts: a review.* Topics in Catalysis, 2016. **59**(15-16): p. 1438-1457.
42. Hill, A.K. and L. Torrente-Murciano, *In-situ H 2 production via low temperature decomposition of ammonia: insights into the role of cesium as a promoter.* International Journal of Hydrogen Energy, 2014. **39**(15): p. 7646-7654.
43. Phanichphant, S., *Semiconductor metal oxides as hydrogen gas sensors.* Procedia Engineering, 2014. **87**: p. 795-802.
44. Prajapati, C. and P. Sahay, *Studies on metal-oxide semiconductor ZnO as a hydrogen gas sensor.* Journal of Nano-and Electronic Physics, 2011. **3**(1): p. 714.
45. Elbohy, H., et al., *Creation of oxygen vacancies to activate WO 3 for higher efficiency dye-sensitized solar cells.* Sustainable Energy & Fuels, 2018.

46. Ramana, C., et al., *Structural stability and phase transitions in WO3 thin films.* The Journal of Physical Chemistry B, 2006. **110**(21): p. 10430-10435.
47. Adhikari, S. and D. Sarkar, *Electrochemical Response for Spherical and Rod Shaped WO_3 Nanoparticles.* ISRN Nanotechnology, 2013. **2013**.
48. Nah, Y.-C., et al., *Nitrogen doping of nanoporous WO3 layers by NH3 treatment for increased visible light photoresponse.* Nanotechnology, 2010. **21**(10): p. 105704.
49. Wang, G., et al., *Hydrogen-treated WO3 nanoflakes show enhanced photostability.* Energy & Environmental Science, 2012. **5**(3): p. 6180-6187.
50. Li, Y.H., et al., *Local atomic structure modulations activate metal oxide as electrocatalyst for hydrogen evolution in acidic water.* Nature communications, 2015. **6**.
51. Qing, R. and W. Sigmund, *Morphological and crystallite size impact on electrochemical performance of electrospun rutile and rutile/multiwall carbon nanotube nanofibers for lithium ion batteries.* Ceramics International, 2014. **40**(4): p. 5665-5669.
52. Bruck, A.M., et al., *Nanocrystalline iron oxide based electroactive materials in lithium ion batteries: the critical role of crystallite size, morphology, and electrode heterostructure on battery relevant electrochemistry.* Inorganic Chemistry Frontiers, 2016. **3**(1): p. 26-40.
53. Sottmann, J., et al., *How Crystallite Size Controls the Reaction Path in Nonaqueous Metal Ion Batteries: The Example of Sodium Bismuth Alloying.* Chemistry of Materials, 2016. **28**(8): p. 2750-2756.
54. Anwar, T., et al., *Effect of Annealing Atmosphere Induced Crystallite Size Changes on the Electrochemical Properties of TiO_2 Nanotubes Arrays.* Journal of Electrical Engineering, 2016. **4**: p. 43-51.
55. Arico, A.S., et al., *Nanostructured materials for advanced energy conversion and storage devices.* Nature materials, 2005. **4**(5): p. 366.
56. Bruce, P.G., B. Scrosati, and J.M. Tarascon, *Nanomaterials for rechargeable lithium batteries.* Angewandte Chemie International Edition, 2008. **47**(16): p. 2930-2946.
57. Karuppasamy, K.M. and A. Subrahmanyam, *Studies on the correlation between electrochromic colouration and the relative density of tungsten trioxide (WO3− x) thin films prepared by electron beam evaporation.* Journal of Physics D: Applied Physics, 2009. **42**(9): p. 095301.
58. Wang, J., et al., *Oxygen vacancy induced band-gap narrowing and enhanced visible light photocatalytic activity of ZnO.* ACS applied materials & interfaces, 2012. **4**(8): p. 4024-4030.
59. Khan, M.E., M.M. Khan, and M.H. Cho, *Fabrication of WO 3 nanorods on graphene nanosheets for improved visible light-induced photocapacitive and photocatalytic performance.* RSC Advances, 2016. **6**(25): p. 20824-20833.
60. Ansari, S.A., et al., *Oxygen vacancy induced band gap narrowing of ZnO nanostructures by an electrochemically active biofilm.* Nanoscale, 2013. **5**(19): p. 9238-9246.
61. Jhan, Y.-R. and J.-G. Duh, *Electrochemical performance and low discharge cut-off voltage behavior of ruthenium doped $Li_4Ti_5O_{12}$ with improved energy density.* Electrochimica Acta, 2012. **63**: p. 9-15.
62. Li, B., et al., *Mesoporous Tungsten Trioxide Polyaniline Nanocomposite as an Anode Material for High-Performance Lithium-Ion Batteries.* ChemNanoMat, 2016. **2**(4): p. 281-289.

63. Yoon, S., et al., *Conductive surface modification of cauliflower-like WO3 and its electrochemical properties for lithium-ion batteries.* Journal of Alloys and Compounds, 2014. **613**: p. 187-192.
64. Chen, J.S., L.A. Archer, and X.W.D. Lou, *SnO_2 hollow structures and TiO_2 nanosheets for lithium-ion batteries.* Journal of Materials Chemistry, 2011. **21**(27): p. 9912-9924.
65. Jo, C., et al., *Tracking the confinement effect of highly dispersive carbon in a tungsten oxide/carbon nanocomposite: conversion anode materials in lithium ion batteries.* Journal of Materials Chemistry A, 2017. **5**(47): p. 24782-24789.
66. Sun, Y., et al., *Graphite-encapsulated Li-metal hybrid anodes for high-capacity Li batteries.* Chem, 2016. **1**(2): p. 287-297.
67. Wang, Z.-L., et al., *In situ fabrication of porous graphene electrodes for high-performance energy storage.* ACS nano, 2013. **7**(3): p. 2422-2430.
68. Wu, Z.-S., et al., *Three-dimensional graphene-based macro-and mesoporous frameworks for high-performance electrochemical capacitive energy storage.* Journal of the American Chemical Society, 2012. **134**(48): p. 19532-19535.
69. Liu, D., et al., *TiO 2 nanotube arrays annealed in N 2 for efficient lithium-ion intercalation.* The Journal of Physical Chemistry C, 2008. **112**(30): p. 11175-11180.
70. Liu, Y., et al., *Self-improving anodes for lithium-ion batteries: continuous interlamellar spacing expansion induced capacity increase in polydopamine-derived nitrogen-doped carbon tubes during cycling.* Journal of Materials Chemistry A, 2015. **3**(42): p. 20880-20885.
71. Liu, Z., et al., *Facile preparation of hexagonal WO 3· 0.33 H 2 O/C nanostructures and its electrochemical properties for lithium-ion batteries.* Applied Surface Science, 2017. **394**: p. 70-77.
72. Li, N., et al., *Battery performance and photocatalytic activity of mesoporous anatase TiO2 nanospheres/graphene composites by template-free self-assembly.* Advanced Functional Materials, 2011. **21**(9): p. 1717-1722.